Energy-loss- and thickness-dependent contrast in atomic-scale electron energy-loss spectroscopy

Haiyan Tan
CEMES-CNRS, Université de Toulouse, nMat Group, BP94347, 31055, Toulouse Cedex 4, France
and Materials Science and Engineering Division, National Institute of Standards and Technology, Gaithersburg, Maryland 20899, USA

Ye Zhu
Monash Centre for Electron Microscopy and Department of Materials Engineering, Monash University, Victoria 3800, Australia

Christian Dwyer*
Ernst Ruska-Centre for Microscopy and Spectroscopy with Electrons,
and Peter Grünberg Institute, Forschungszentrum Jülich, D-52425 Jülich, Germany

Huolin L. Xin†
Center for Functional Nanomaterials, Brookhaven National Laboratory, Upton, New York 11973, USA
(Received 7 October 2014; revised manuscript received 8 December 2014; published 31 December 2014)

Atomic-scale elemental maps of materials acquired by core-loss inelastic electron scattering often exhibit an undesirable sensitivity to the unavoidable elastic scattering, making the maps counterintuitive to interpret. Here, we present a systematic study that scrutinizes the energy-loss and sample-thickness dependence of atomic-scale elemental maps acquired using 100-keV incident electrons in a scanning transmission electron microscope. For single-crystal silicon, the balance between elastic and inelastic scattering means that maps generated from the near-threshold Si-L signal (energy loss of 99 eV) show no discernible contrast for a thickness of 0.5λ (λ is the electron mean-free path, here approximately 110 nm). At greater thicknesses we observe a counterintuitive "negative" contrast. Only at much higher energy losses is an intuitive "positive" contrast gradually restored. Our quantitative analysis shows that the energy loss at which a positive contrast is restored depends linearly on the sample thickness. This behavior is in very good agreement with our double-channeling inelastic scattering calculations. We test a recently proposed experimental method to correct the core-loss inelastic scattering and restore an intuitive "positive" chemical contrast. The method is demonstrated to be reliable over a large range of energy losses and sample thicknesses. The corrected contrast for near-threshold maps is demonstrated to be (desirably) inversely proportional to sample thickness. Implications for the interpretation of atomic-scale elemental maps are discussed.

DOI: 10.1103/PhysRevB.90.214305 PACS number(s): 34.80.Dp, 79.20.Uv, 68.37.Ma

I. INTRODUCTION

Atomic-resolution core-loss inelastic scattering in a scanning transmission electron microscope (STEM) is a powerful tool for resolving the local elemental composition and electronic bonding states in materials [1–7]. However, due to the strong interaction of the incident electrons with the material, spatially resolved inelastic scattering is always modified to some extent by the unavoidable elastic scattering, even in relatively thin samples [8,9]. This modification is often evident in atomic-scale elemental maps. For example, inelastic scattering signals of unexpected strengths [2,10], "volcano" patterns around heavy atomic columns [9,11–13], and "negative" contrast where the atomic columns appear "dark" [14,15] have all been observed experimentally. Such effects imply that an atomic-scale elemental map does not necessarily reflect the atomic-scale elemental distribution in the material, especially if the sample contains heavy elements or the core-loss signal lies at an energy loss of less than a few hundred electronvolts [12,16]. Hence in such cases electron scattering simulations are often needed to gain a reliable interpretation [2,9,12,14,15,17–19].

In this article, we present a systematic study of the contrast in atomic-scale elemental maps acquired using core-loss electron energy-loss spectroscopy (EELS) in the STEM. Specifically, we perform a detailed analysis of Si-L maps of single-crystal silicon for both a wide range of energy losses and a large range of sample thicknesses. Our results show that, for moderately thin samples (0.5λ, $\lambda \approx 110$ nm for the beam energy used here), the Si-L maps exhibit practically no contrast for energy losses within the first 40 eV of the Si-$L_{2,3}$ edge onset. For thicker samples (up to 1.6λ), the contrast is negative at the edge onset and evolves to become positive at higher energy losses, which is in agreement with earlier observations [14]. The energy loss at which the contrast changes from negative to positive is demonstrated to be linearly dependent on the sample thickness, a result which is also supported by our double-channeling simulations.

Following our analysis of the counterintuitive contrast, we assess a recently proposed method [19] to correct core-loss maps and restore an intuitive "positive" elemental contrast. This method is demonstrated to yield reliable results over the entire (large) range of energy losses and thicknesses studied here, i.e., up to energy losses of 600 eV beyond threshold and sample thicknesses up to 1.5λ. Our detailed observations of the

*c.dwyer@fz-juelich.de
†hxin@bnl.gov

counterintuitive contrast in atomic-resolution elemental maps, and how to correct it, should be of great value in guiding future STEM-EELS investigations on unknown specimens.

II. METHODS

A TEM lamella of [110]-oriented single-crystal silicon was prepared for observation by focused ion-beam milling. Single-crystal silicon was chosen because it allows a relatively easy acquisition of spectral images with good signal-to-noise ratios (SNRs). Silicon is also a relatively weak scatterer, so that the contrast reversal develops slowly with increasing thickness, which allows a concurrent investigation of the effects of plural inelastic scattering. In addition, a pure silicon sample means that the extended Si-L edge is not interrupted by other edges, allowing us to study the contrast over a wide range of energy losses.

The microscope used for our study is an aberration-corrected Nion UltraSTEM operated at 100 kV. Our experiments used a probe convergence semiangle of 32 mrad, producing a probe size of approximately 0.1 nm. The two-dimensional (2D) electron energy-loss spectrum images (SIs) (which consist of a spectrum for each 2D probe position x,y) were recorded using a Gatan Enfina spectrometer using a collection semiangle of 80 mrad. The energy dispersion and dwell time were set to 0.5 eV/channel, 10 ms/pixel for core loss and 0.1 ms/pixel for low loss, respectively. The field of view for each EELS map was $1.8 \times 1.8\,\mathrm{nm}^2$, recorded using 64×64 probe positions. Annular dark-field (ADF) images were acquired simultaneously with the SIs using inner and outer semiangles of 98 and 295 mrad, respectively.

Low-loss SIs were acquired from the same sample area immediately after the core-loss SI's acquisition. In post-processing of the data, the low- and core-loss SIs were corrected for sample drift and aligned atomic column-by-atomic column. The low- and core-loss SIs were spliced together following this procedure. The low-loss spectra were used to compute the sample thicknesses from the ratio of elastic and inelastic scattering [20]. The low-loss spectra also enable the deconvolution of core-loss signal (described below).

The background intensity under the Si-L edge was removed by subtracting the extrapolated pre-edge intensity. One of the challenges of this procedure is that the results exhibit some dependence on the pre-edge energy window and the model used for extrapolation. This is especially the case in the present work where we are interested in signals lying several hundred electronvolts above the Si-L edge onset. However, our tests showed that reasonable variations in the background model and fitting window result in only subtle changes to the subtracted Si-L edge intensity and the contrast. Moreover, the subtracted Si-L intensities exhibit very good agreement with accurate inelastic scattering calculations (described below). Hence we conclude that the background subtraction procedure is working sufficiently well. Ultimately, we used a power-law model and a 30-eV pre-edge window to extrapolate and then remove the background under the Si-L edge for each individual spectrum. The Si-L signal was then integrated over the chosen energy window. The result is a single value, representing the inelastic scattering signal, at each probe position. In this work, we used energy windows 20 eV wide, centered at various energy losses in order to investigate the energy dependence of the resulting maps.

For a quantitative analysis of the contrast, spectra at probe positions across each of the Si dumbbells in the field of view were extracted from the 2D SI, resulting in a set of one-dimensional (1D) "line-scan" SIs. These 1D SIs were then averaged to enhance the SNR. Letting $I(E,x)$ denote the intensity in an averaged 1D SI (E is energy loss, x is 1D probe position), the intensities were rescaled according to $C(x,E) = I(x,E)/\langle I(x,E)\rangle_x - 1$, where the average is taken over x in 2 unit cells range. Since a positive (negative) value of $C(x,E)$ corresponds to an intensity which is greater (less) than the average intensity, we refer to $C(E,x)$ as the "contrast." In our analysis, we mainly considered the contrast for probe positions atop a Si atomic column (on-column), since such positions would ideally reflect the chemical distribution of the atomic sites in our sample.

In addition to analyzing the contrast of the Si-L signal as described above, we also examined the use of both Fourier-ratio and Fourier-log deconvolution with the low-loss spectra as a means of removing the effects of multiple inelastic scattering. These deconvolution procedures were carried out on the 2D as-acquired SIs and the 1D-averaged SIs using DIGITAL MICROGRAPH. Both flavors of deconvolution yield similar results, so that here only the Fourier-ratio deconvolution results are presented. As a supplementary step to the deconvolution procedures implemented in DIGITAL MICROGRAPH, we apply a scaling factor $I_{\mathrm{total}}/I_{\mathrm{ZLP}}$ (ZLP: zero-loss peak) in order to restore the correct intensity in the single-scattered signals [21]. This scaling factor exhibited atomic-scale fluctuations corresponding to $\pm 0.02\lambda$, arising from the different channeling conditions for probes positioned on or off the Si atomic columns.

Correction of the Si-L signal to restore an intuitive chemical contrast followed the procedure described in our previous work [19]. In essence, the method consists of dividing the EELS map by a "correction map" which is derived from the zero- and low-loss intensity. This procedure has the effect of compensating for the majority of elastic and low-loss events that cause the Si-L signal to be scattered beyond the EELS collection aperture. The main prerequisite for the validity of this procedure is that the collection aperture is large enough to average out the majority of coherent scattering effects. This condition is amply satisfied by the collection angle used here. The correction procedure was applied to the individual spectra in the spliced SIs. The Si-L signals were then extracted and the contrast calculated as described above.

The simulations in this work are based on a multislice solution to Yoshioka's equations [22] for the dynamical elastic and inelastic scattering of high-energy electrons. The approach [23] includes multiple elastic scattering, multiple thermal diffuse scattering based on a frozen phonon approximation [24,25], and single inelastic scattering due to atomic core-level excitations. Elastic and thermal diffuse scattering both before and after each core excitation event, referred to as double channeling, was included. The simulated Si-L maps were performed on a general-purpose graphic processing (GPGPU) code similar to that described in our previous work [26]. The matrix elements for excitation of the Si-L shell were calculated using atomic wave functions

obtained from the Cowan code [27]. The use of atomic wave functions means that solid-state effects are neglected. For each Si atom, transitions to final (continuum) atomic states with orbital quantum numbers $l = 0$, 1, 2, and 3 were considered. (The contributions of transitions to higher-order states are negligible.) To reduce the time required for the double-channeling calculations, a reduction of the total number of transitions was performed by including only those transitions which constitute the first 95% of the single channeling intensity (where scattering after a core excitation is neglected) and then rescaling the resulting double-channeling intensity, as described previously [28]. The simulations used a supercell of size $3.07 \times 3.26\,\text{nm}^2$, sampled using 512×512 pixels. The beam energy, probe-convergence, and collection semiangles were chosen to match the experimental conditions. Source size effects were included in the simulations by convoluting the simulated maps with a source function. The source of our instrument is described by a Gaussian with a FWHM of 0.71 Å convolved with a truncated Lorentzian with a FWHM of 0.18 Å, as published previously [9].

III. RESULTS AND DISCUSSION

A. Experimental analysis of atomic-scale contrast

Figure 1(a) shows the energy-loss spectra of Si crystals with thicknesses of 0.5λ, 1.0λ, and 1.5λ. The corresponding Si-L spectra, which begin at an energy loss of 99 eV, are shown in Fig. 1(b). As the thickness increases, increased plural inelastic scattering causes the multiple-plasmon peaks to become more evident, while the signal-to-background ratio (SBR) at the Si-L onset is seen to drop dramatically. The areas shown in blue illustrate the energy-integration windows used to generate the Si-L maps in Fig. 2.

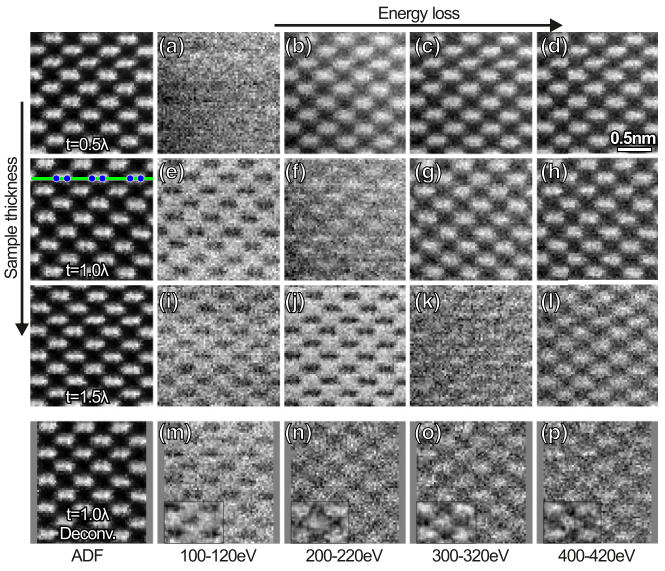

FIG. 2. (Color online) Atomic-resolution Si-L maps at different energy losses and sample thicknesses (a–l). For a thickness of 1λ, maps derived after deconvolution are also shown (m–p), where the insets show the results of low-pass Gaussian filtering with a FWHM of 0.04 nm. The simultaneously acquired ADF images are shown on the left.

Figure 2 shows Si-L maps generated at various energy losses and sample thicknesses. Under these experimental conditions the simultaneously acquired ADF images (Fig. 2,

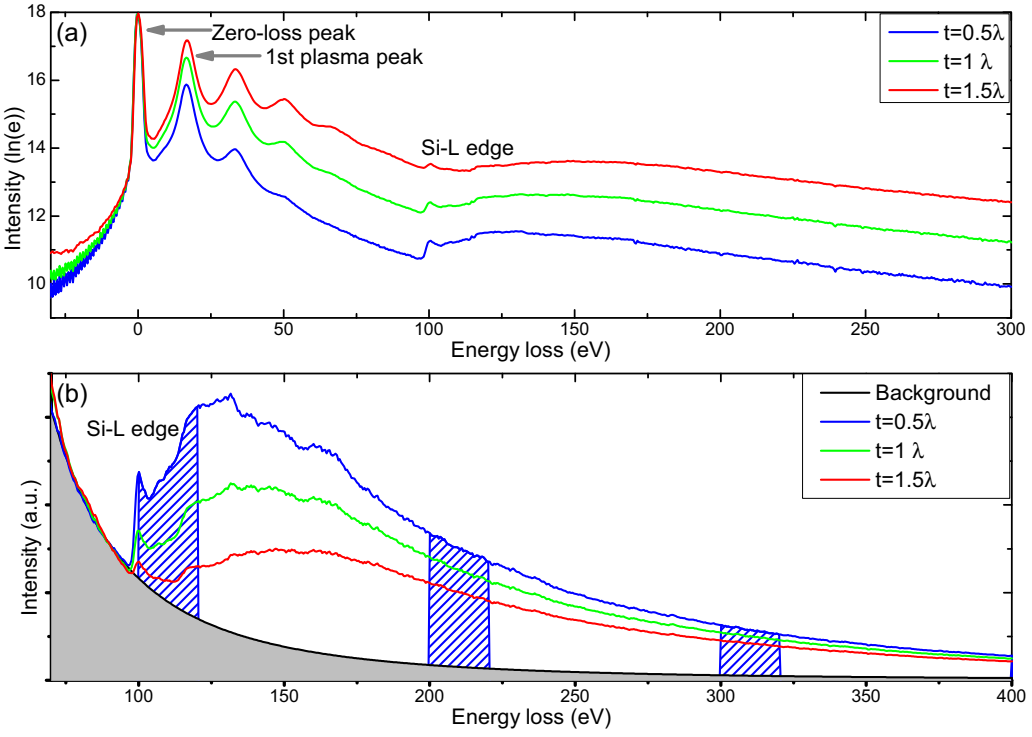

FIG. 1. (Color online) (a) The energy-loss spectra of Si crystals for various thicknesses (log scaling). (b) The Si-L core-loss spectrum (linear scaling). After subtraction of power-law background (gray), the Si-L signal is integrated over 20-eV energy windows (shown in blue for the 0.5λ case) to produce the maps shown in Fig. 2.

left column) provide a robust representation of the atomic structure, whereby the "dumbbell" structure, characteristic of the [110] orientation, is well resolved. Although the elemental maps are also typically expected to resemble the underlying atomic-scale elemental distribution, here this is often not the case. Comparing them with the ADF images, the maps exhibit various types of contrast, including reversed contrast, i.e., "dark" atomic columns, over a significant proportion of the energy-thickness range. For a thickness of 0.5λ, the near-threshold map (100 eV) shows no contrast other than noise [Fig. 2(a)]. Not until the energy loss is increased to 210 eV does the map reflect the elemental distribution [Fig. 2(b)]. The contrast and spatial resolution are further improved at higher energy losses [Figs. 2(c) and 2(d)]. For an energy loss of 410 eV, the map reveals the Si dumbbell structure and hence demonstrates a spatial resolution comparable to the ADF image (Fig. 2, top left). This behavior with respect to energy loss is due to inelastic delocalization, which is highly prominent at the Si-L onset, but decreases with increasing energy loss [20], providing better spatial resolution. Similar effects have been reported by Kimoto *et al.* [29] for Si maps of β-Si_3N_4 and Botton *et al.* [12] for Sr maps of $SrTiO_3$. For the sample thickness of 1λ, the Si-L map at onset shows negative contrast [Fig. 2(e)]. This negative contrast gradually fades with increasing energy loss until it disappears at about 210 eV [Fig. 2(f)]. At higher losses, the contrast becomes positive and continues to increase [Figs. 2(g) and 2(h)]. For the thickest sample (1.5λ), the behavior is similar, except that the change from negative to positive contrast occurs at about 310 eV [Fig. 2(k)]. Overall, the contrast tends from negative to positive with increasing energy loss, and tends from positive to negative with increasing thickness.

One might suspect that the thickness-dependent contrast reversal is due to plural inelastic scattering. After careful Fourier-ratio deconvolution of the 1.0λ data, the contrast at the Si-L onset still remains negative (Fig. 2 m), while the map at 200 eV has retained positive chemical contrast. This implies that the plural inelastic scattering involving plasmon excitations is not the main cause of the contrast reversal. As a matter of fact, Fourier-ratio deconvolution does little to change the shape of the Si-L spectrum near onset (apart from an overall scaling described in Sec. II). Hence very little change in the map at edge onset is expected. We note that the deconvoluted results exhibit greater noise compared to the pristine (not deconvoluted) results, which is a drawback of the deconvolution process [20]. A low-pass filter can reduce this noise, but at the cost of reducing the spatial resolution and contrast [Figs. 2(m)–2(p) insets].

Figure 3(a) shows the averaged line-scan SI for probe positions across the Si dumbbell in the 1λ-thick sample (probe positions indicated by the green line in Fig. 2, left column). Its contrast image [Fig. 3(b)] shows an obvious reversal at an energy loss of 210 eV (indicated by the black dashed vertical line). The energy loss at which the reversal occurs, which we denote by E_R, has a strong dependence on sample thickness. In line with the results in Fig. 2, the contrast of deconvoluted SI [Fig. 3(c)] remains negative near the edge onset. For the deconvoluted SI, E_R (red vertical dashed line) is approximately 45 eV less than that of the pristine SI. Figure 3(e) shows that deconvolution has small effect on the contrast near onset but

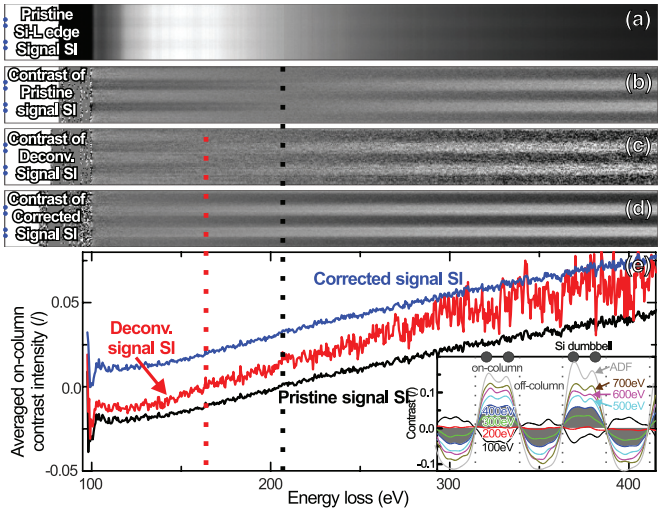

FIG. 3. (Color online) Analysis of contrast as a function of energy loss for an averaged "line-scan" SI crossing Si dumbbells ($t = 1\lambda$). (a) Pristine Si-L SI. (b) Contrast image of the pristine SI shown in (a). (c) Contrast image of the deconvoluted SI. (d) Contrast image of the corrected SI. (e) On-column contrast of the pristine (black), deconvoluted (red), and corrected SIs. Dotted drop lines (black and red) indicate the energy losses corresponding to a contrast reversal of the pristine and deconvoluted signal SI, respectively. The on-column contrast is the average of those positions where the Si-L signal exceeds its average value, as shown by the inset for 400-eV energy loss. The inset shows line profiles of the ADF and Si-L signals (various energy losses) for probe positions across the Si dumbbells.

enhances the contrast at high energy losses. The enhancement can be attributed to the restoration of the more-localized core-loss signal, which is otherwise shifted to higher energy losses by plural inelastic scattering. The result in Fig. 3(d) will be discussed later.

The inset of Fig. 3(e) shows pristine line profiles for energy losses 100–700 eV, providing further clarification of the behavior. Briefly, the 100-eV profile is inverted with respect to the ADF profile; the 200-eV profile has essentially zero contrast; higher-loss profiles are qualitatively similar to the ADF profile; the Si dumbbell structure can be seen from 400 eV onwards.

The behavior of the on-column contrast is summarized in Fig. 4. The increasingly negative contrast for thicker samples is clearly seen, as is the corresponding increase in E_R (indicated by dropping arrows).

Figure 5 summarizes the behavior of E_R as a function of sample thickness, for both pristine and deconvoluted data. Within the range of thicknesses investigated, the pristine case is well fitted by the linear relationship $E_R = 145.3\tau + 60.6$, where τ is the sample thickness in units of the electron mean-free path (black line). This relationship provides a straightforward way to estimate the minimum energy loss required for a positive-contrast map. Alternatively, one can also use this relationship to estimate the sample thickness if the contrast-reversal energy is known. For the deconvoluted case, E_R is well fitted by $E_R = 86.4\tau + 78.4$ (red line). For thin samples, where deconvolution has relatively little effect, the pristine and deconvoluted E_R values essentially coincide.

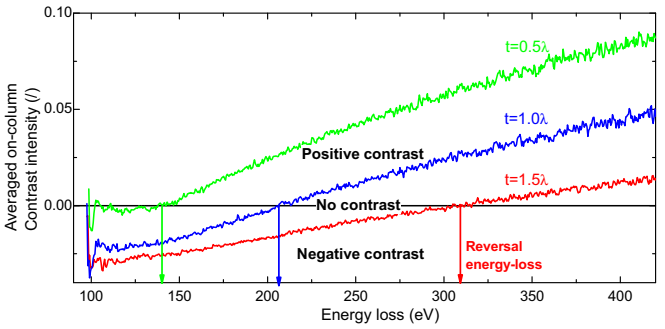

FIG. 4. (Color online) The on-column contrast in the pristine Si-L maps plotted as a function of energy loss for samples thickness of 0.5λ, 1λ, and 1.5λ. The dropping arrows indicate energy losses corresponding to a contrast reversal.

On the other hand, at a thickness of 1.6λ, the difference in E_R can be as high as 90 eV. These results can be summarized by stating that the plural inelastic scattering has the effect of "postponing" the restoration of positive contrast.

B. Theoretical-based interpretation of contrast

The results from our double-channeling calculations are also plotted in Fig. 5. (While here we do not show the simulated maps themselves, their appearance is in excellent agreement with the experimental maps in Fig. 2, which is in accord with the agreement obtained in our previous investigations [9,12,15,19].) In Fig. 5, the qualitative trend of the simulation agrees very well with the experimental results, especially the deconvoluted data sets. The better agreement with deconvoluted data is expected, since the simulations do not take into account the effects of plural inelastic scattering. The simulation predicts an increase in the reversal energy with increasing thickness that is in good accord with experiment. Quantitatively, the reversal energies predicted by the simulation are about 25 eV lower. The precise cause of the discrepancy remains to be resolved, though plausible reasons include residual inaccuracies in the experimental background estimation, inaccuracy of the

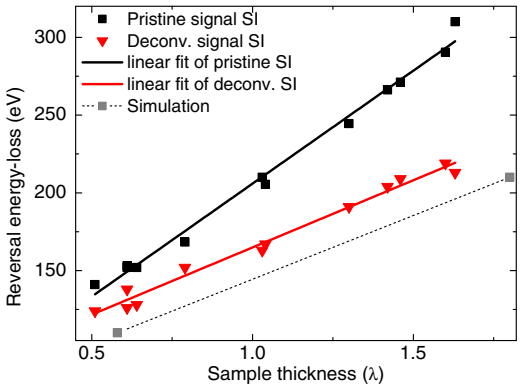

FIG. 5. (Color online) The Si-L edge contrast-reversal energy loss E_R as a function of sample thickness, as determined experimentally from the pristine and deconvoluted signal SIs. The gray points indicate the prediction of double-channeling simulations.

deconvolution procedures applied to the experimental data, or inaccuracies in the simulation resulting from the single-electron description of the core-loss process. Despite the (relatively small) discrepancy, the simulations provide a very good account of the important scattering processes, and thus provide important insight into the origins of counterintuitive contrast.

From an analysis of our simulations, we conclude that the contrast behavior with energy loss and thickness is associated with:

(1) The elastic scattering behavior of the electron probe. For probe positions on top of a Si column, elastic and thermal-diffuse scattering leads, at shallow sample depths, to an increased probe amplitude on the atomic column (i.e., channeling), while at greater sample depths it leads to a depletion of the probe amplitude in the vicinity of the column (i.e., dechanneling). On the other hand, for off-column positions, the probe amplitude tends to disperse with increasing depth, though it largely remains between the columns [30].

(2) The Si-L matrix elements. The matrix elements describing excitations at the Si-L threshold are relatively broad (FWHM $\approx$ 0.3 nm), due to inelastic delocalization at this relatively small (99 eV) threshold energy. Importantly, these matrix elements are much broader than the electrostatic potential of a Si column (FWHM $\approx$ 0.04 nm), which is responsible for the elastic scattering behavior discussed above. As the energy loss increases, the matrix elements become significantly narrower (FWHM $\approx$ 0.08 nm at an energy loss of 400 eV).

(3) Double-channeling. If the Si-L inelastic scattering originates in the immediate vicinity of an atomic column, then subsequent elastic scattering can further enhance the preservation of the elastic contrast [9,15,31].

1. Thickness behavior

For on-column positions, the channeling-dechanneling behavior leads to a strong Si-L signal from the Si atoms at shallow depths, and a weak signal from atoms at greater depths. This effect is largely independent of the energy loss. For off-column positions and energy losses near onset, the broad matrix elements mean that the Si-L signal can still be relatively strong. For thin samples, these effects give rise to a Si-L map that, while peaked at the Si columns, has very low contrast because the off-column signal is relatively strong. In thicker samples, due to the dechanneling of the probe and the double-channeling effect, the on-column signal is exceeded by the off-column one, leading to a map with negative contrast.

2. Energy-loss behavior

As the energy loss increases beyond the onset, the narrowing of the matrix elements reduces the off-column signal [14]. Eventually, for large enough energy losses, the off-column signal is reduced to the point where a contrast reversal is no longer observed for any reasonable sample thickness.

C. Restoration of chemical contrast

In this final section, we test the recently proposed method [19] to overcome the counterintuitive contrast resulting

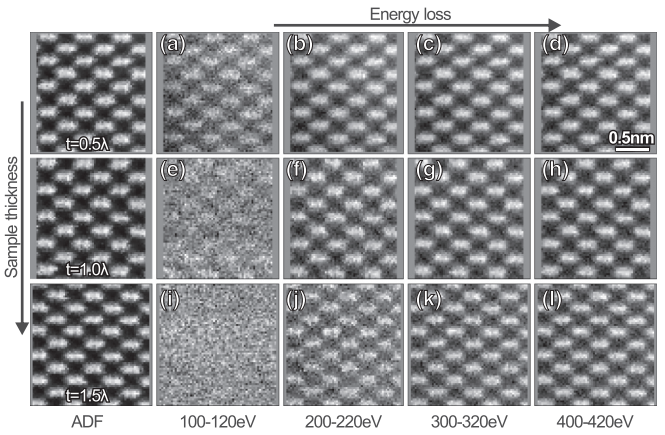

FIG. 6. Corrected atomic-resolution Si-L maps at different energy losses and sample thicknesses (a–l). The simultaneously acquired ADF images are shown on the left. The maps exhibit intuitive chemical contrast in all cases, except in (i) where the map is dominated by noise.

from elastic and thermal diffuse scattering, as described in the Experimental section. Due to the increased noise resulting from deconvolution, the correction procedure has been performed on the pristine data only.

The corrected maps for different sample thicknesses and energy losses are shown in Fig. 6. Comparing with the uncorrected maps in Fig. 2, we see that the corrected maps exhibit a marked absence of contrast reversals, and, moreover, display an intuitive chemical contrast with intensity peaks located at the positions of the Si atomic columns. The only exception to this behavior is the corrected map in Fig. 6(i), where the contrast becomes dominated by noise.

A further analysis of the corrected maps is shown in Figs. 3(d) and 3(e), which display the average contrast across the Si dumbbells as a function of energy loss in the 1λ-thick sample. It is readily seen that the contrast of the corrected SI is positive across the entire range of energy losses, and increases with energy loss at a rate that is very similar to the pristine SI [Fig. 3(e)]. Importantly, the level of noise in the corrected SI is comparable to the pristine SI, implying that the correction procedure does not introduce significant noise. This can be understood from the fact that the correction is derived from the combined zero- and low-loss signals, and hence has a very high SNR.

Figure 7 compares the corrected and pristine on-column contrasts as a function of energy loss and thickness. Once again, in marked difference to the pristine case, we observe that the corrected on-column contrast is positive in all cases. The contrast generally decreases with increasing thickness across the entire range of energy losses. Near threshold, the contrast decreases nearly to zero for a thickness of 1.5λ, in agreement with the appearance of the corrected map in Fig. 6(i).

A further scrutiny of the corrected contrast near threshold is presented in Fig. 8. There we see that the contrast is decreasing with respect to sample thickness, with a relationship that is well fitted by the simple linear relationship $C_{\text{onset}} = -0.015\tau + 0.028$. Similar linear relationships apply at higher energy losses (not shown). Remarkably, such an inverse relationship between contrast and sample thickness is expected in the

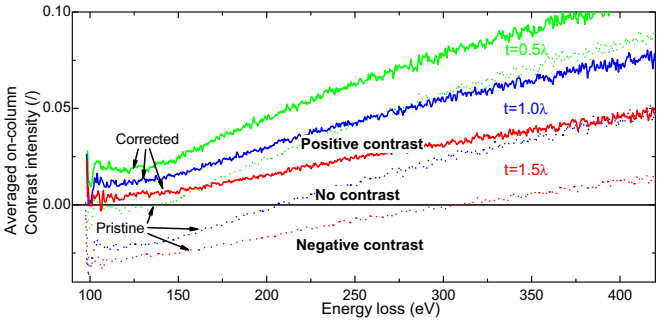

FIG. 7. (Color online) A comparison of the pristine (dotted lines) and corrected (solid lines) on-column contrasts as a function of energy loss for samples thickness of 0.5λ, 1λ, and 1.5λ. The corrected contrast is positive for all energy losses and thicknesses.

absence of elastic and thermal diffuse scattering, where the electron beam would spread nearly geometrically with increasing thickness. Hence, at least for the case studied here, our results indicate that the correction procedure removes the counterintuitive contrast resulting from elastic and thermal diffuse scattering in a way that is close to ideal.

Although here we have applied the correction procedure to remove counterintuitive contrast in maps of a specimen containing relatively light atomic columns (Si), we emphasize that the method is not restricted to such cases. For example, in the work of Zhu *et al.* [19] the method was applied to the Ba-N maps in $BaTiO_3$ and was verified to produce excellent results up to sample thicknesses of 100 nm. Hence those examples, along with the present example, demonstrate that this method is applicable to both light and heavy atomic columns.

We also wish to draw a comparison with an alternative procedure for removing elastic and thermal diffuse scattering effects from electron energy-loss spectra proposed by Lugg *et al.* [32]. Their method has the advantage of removing these effects from the individual spectra, enabling access to both elemental maps and energy-loss near-edge structure, for example. However, their method also has the rather serious drawback that the exact atomic structure of the specimen must already be known. By contrast, the (considerably simpler)

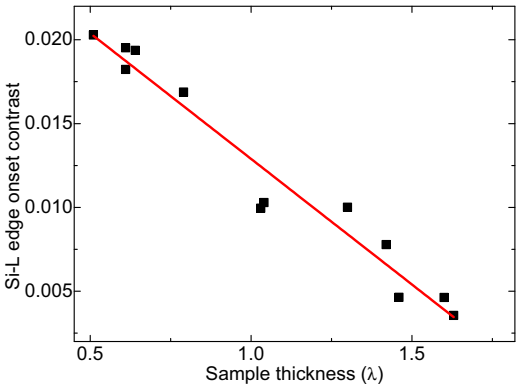

FIG. 8. (Color online) The corrected on-column contrast at the edge onset (energy losses of 100–110 eV). The contrast is well-fitted by a linear relationship.

method demonstrated here is aimed at removing the counterintuitive effects of elastic and thermal diffuse scattering in atomic-resolution elemental maps (not individual spectra), and it does not require any assumptions about the atomic structure of the specimen.

IV. CONCLUSION

Using aberration-corrected atomic-resolution STEM-EELS, we have investigated the contrast of Si-L maps acquired from [110] silicon over a wide range of energy losses and sample thicknesses. We have conclusively demonstrated that maps generated directly from energy losses near the Si-L onset do not reflect, even qualitatively, the underlying atomic-scale elemental distribution for moderate or greater sample thicknesses ($>0.5\lambda$). Maps representative of the elemental distribution are obtained only for energy losses of at least 40–200 eV above onset, depending on the sample thickness. Lower losses usually lead to maps with either no specific contrast or negative contrast. The relationship between the energy loss at which contrast reversal occurs and the sample thickness was found to be well described by a linear function, which offers a useful guide for future studies on unknown samples. These findings were found to be in good agreement with double-channeling simulations, which were then used to offer insight into this phenomena.

We also presented a rigorous test of a recently proposed method to correct for the counterintuitive effects of elastic and thermal diffuse scattering and restore positive chemical contrast. The method was demonstrated to perform very well over the entire range of thicknesses and energy losses. After the correction, the Si-L maps provide an excellent qualitative representation of the atomic-scale elemental distribution. Together with our previous results [19], these results demonstrate that the method is applicable to materials containing light and/or heavy atoms, and can be used for sample thicknesses up to at least one inelastic mean-free path (and is likely applicable at even greater thicknesses).

Finally, it is anticipated that similar results, regarding both counterintuitive contrast and its correction, will be obtained for core-loss maps of other materials at similar energy losses. We anticipate that the correction procedure will be highly beneficial in such cases. At higher energy losses, the increased localization of the inelastic scattering means that the observation of negative contrast becomes less likely. In these cases the effect of the correction procedure is likely to be less dramatic, although still potentially useful.

ACKNOWLEDGMENTS

H.T. acknowledges financial support from Centre d'Elaboration de Matériaux et d'Etudes Structurales, CNRS, and National Institute of Standards and Technology, USA. Y.Z. and C.D. gratefully acknowledge financial support from the Australian Research Council (Grant No. DP110104734). C.D. acknowledges support from the Ernst Ruska Centre. H.L.X. acknowledges support from Center for Functional Nanomaterials, Brookhaven National Laboratory, which is supported by the U.S. Department of Energy, Office of Basic Energy Sciences, under Contract No. DE-AC02-98CH10886. This work made use of the electron microscopy facility of the Cornell Center for Materials Research (CCMR) with support from the National Science Foundation Materials Research Science and Engineering Centers (MRSEC) program (Contract No. DMR 1120296). Experimental data recording, and H.L.X. for that period, was supported by the Energy Materials Center at Cornell (emc2), an Energy Frontier Research Center funded by the U.S. Department of Energy, Office of Basic Energy Sciences, under Award No. DESC0001086. H.L.X. also thanks David A. Muller for his support and advice on this project. Correspondence and requests for materials should be addressed to C.D. and H.L.X.

[1] K. Kimoto, T. Asaka, T. Nagai, M. Saito, Y. Matsui, and K. Ishizuka, Nature (London) **450**, 702 (2007).

[2] M. Bosman, V. J. Keast, J. L. García-Muñoz, A. J. DAlfonso, S. D. Findlay, and L. J. Allen, Phys. Rev. Lett. **99**, 086102 (2007).

[3] D. A. Muller, Nat. Mater. **8**, 263 (2009).

[4] H. Tan, S. Turner, E. Yücelen, J. Verbeeck, and G. Van Tendeloo, Phys. Rev. Lett. **107**, 107602 (2011).

[5] G. A. Botton, MRS Bull. **37**, 21 (2012).

[6] J. A. Mundy, Q. Mao, C. M. Brooks, D. G. Schlom, and D. A. Muller, Appl. Phys. Lett. **101**, 042907 (2012).

[7] H. Tan, R. Egoavil, A. Béché, G. T. Martinez, S. Van Aert, J. Verbeeck, G. Van Tendeloo, H. Rotella, P. Boullay, A. Pautrat, and W. Prellier, Phys. Rev. B **88**, 155123 (2013).

[8] A. Howie, Proc. R. Soc. London, Ser. A **271**, 268 (1963).

[9] H. L. Xin, C. Dwyer, and D. A. Muller, Ultramicroscopy **139**, 38 (2014).

[10] K. Dudeck, M. Couillard, S. Lazar, C. Dwyer, and G. Botton, Micron **43**, 57 (2012).

[11] H. Kohl and H. Rose, *Theory of Image Formation by Inelastically Scattered Electrons in the Electron Microscope,* edited by P. Hawkes, Advances in Electronics and Electron Physics (Academic Press, London, 1985), pp. 173–227.

[12] G. Botton, S. Lazar, and C. Dwyer, Ultramicroscopy **110**, 926 (2010).

[13] S. Lazar, Y. Shao, L. Gunawan, R. Nechache, A. Pignolet, and G. A. Botton, Microsc. Microanal. **16**, 416 (2010).

[14] P. Wang, A. J. D'Alfonso, S. D. Findlay, L. J. Allen, and A. L. Bleloch, Phys. Rev. Lett. **101**, 236102 (2008).

[15] C. Dwyer, H. L. Xin, and D. A. Muller, Phys. Rev. B **86**, 094119 (2012).

[16] L. F. Kourkoutis, H. Xin, T. Higuchi, Y. Hotta, J. Lee, Y. Hikita, D. Schlom, H. Hwang, and D. Muller, Philos. Mag. **90**, 4731 (2010).

[17] M. P. Oxley, M. Varela, T. J. Pennycook, K. van Benthem, S. D. Findlay, A. J. D'Alfonso, L. J. Allen, and S. J. Pennycook, Phys. Rev. B **76**, 064303 (2007).

[18] A. J. D'Alfonso, S. D. Findlay, M. P. Oxley, and L. J. Allen, Ultramicroscopy **108**, 677 (2008).

[19] Y. Zhu, A. Soukiassian, D. G. Schlom, D. A. Muller, and C. Dwyer, Appl. Phys. Lett. **103**, 141908 (2013).

[20] R. F. Egerton, *Electron Energy-Loss Spectroscopy in the Electron Microscope*, 3rd ed. (Springer, New York, 2011).
[21] Y. Zhu and C. Dwyer, Microsc. Microanal. **20**, 1070 (2014).
[22] H. Yoshioka, J. Phys. Soc. Japan **12**, 618 (1957).
[23] C. Dwyer, Ultramicroscopy **104**, 141 (2005).
[24] R. F. Loane, P. Xu, and J. Silcox, Acta Crystallogr., Sect. A: Found. Crystallogr. **47**, 267 (1991).
[25] *Advanced Computing in Electron Microscopy*, edited by E. Kirkland, 2nd ed. (Springer, New York, 2010).
[26] C. Dwyer, Ultramicroscopy **110**, 195 (2010).
[27] R. D. Cowan, *The Theory of Atomic Structure and Spectra* (University of California Press, Berkeley and Los Angeles, 1981).
[28] C. Dwyer, S. D. Findlay, and L. J. Allen, Phys. Rev. B **77**, 184107 (2008).
[29] K. Kimoto, K. Ishizuka, and Y. Matsui, Micron **39**, 257 (2008).
[30] C. Dwyer and J. Etheridge, Ultramicroscopy **96**, 343 (2003).
[31] S. L. Cundy, A. Howie, and U. Valdré, Philos. Mag. **20**, 147 (1969).
[32] N. R. Lugg, M. Haruta, M. J. Neish, S. D. Findlay, T. Mizoguchi, K. Kimoto, and L. J. Allen, Appl. Phys. Lett. **101**, 183112 (2012).